Tailoring the transport coefficients and thermoelectric properties of $Cs_2NaYbCl_6$ perovskite by doping and nanoengineering: A first-principles based theoretical approach

Antonio Cappai,* Claudio Melis, and Luciano Colombo
Department of Physics, University of Cagliari, Cittadella Universitaria, I-09042 Monserrato (CA), Italy

(Received 6 August 2025; accepted 26 November 2025; published 20 January 2026)

We present a first-principles investigation of the combined effects of chemical doping and nanostructuring on the thermoelectric performance of the double halide perovskite $Cs_2NaYbCl_6$. Using density functional theory and Boltzmann transport calculations, we explicitly include all relevant scattering mechanisms (namely, electron–phonon, phonon–phonon, Coulomb impurity, phonon–impurity, and grain boundary scattering) to evaluate electrical and thermal transport coefficients. Our results show that Coulomb scattering from dopants is strongly screened and negligible compared to dominant electron–phonon interactions. Thus, both *n*- and *p*-type doping enhance electrical conductivity while only moderately reducing the Seebeck coefficient, leading to a significant increase in power factor. Phonon–impurity scattering is found to be minimal, while grain boundary scattering effectively reduces lattice thermal conductivity without strongly affecting carrier mobility. Combining optimal *n*-type doping (10^{19} cm^{-3}) with nanoscale grains (10 nm), the figure of merit ZT increases from $\sim 10^{-8}$ in the pristine crystal to $\sim$0.12. These findings demonstrate a viable pathway for improving thermoelectric efficiency in wide-band-gap, lead-free perovskites through controlled extrinsic modifications.

DOI: 10.1103/729y-m77y

I. INTRODUCTION

The search for high-performance thermoelectric materials is of great interest in modern materials physics, strictly related to fundamental questions about the microscopic mechanisms of charge and heat transport, mutually interacting and enabling the direct conversion of heat in voltage differences. This issue, inherently of fundamental interest, is also of practical relevance within the framework of the so-called green transition: The direct conversion of thermal gradients into electrostatic field shows great potentials for improving the efficiency of existing energy systems. For instance, it could enable the recovery of waste heat that would otherwise be lost to the environment—a scenario that applies not only to traditional thermal power plants, but also to photovoltaics, where thermoelectric cooling [1] could help mitigate temperature increases known to impair device performance.

One of the key limitations still hindering the large-scale implementation of thermoelectric technology lies in the relatively low conversion efficiencies of the best-performing materials available today. Even more concerning is the fact that these materials often rely on toxic elements such as lead, which pose serious environmental concerns. As a result, significant efforts are being directed toward the identification of alternative compounds that could meet the stringent requirements of an ideal thermoelectric material. According to the well-known definition by Slack [2,3], such a material should behave as a "phonon glass" and an "electron crystal", i.e., it should simultaneously exhibit low thermal conductivity and high electrical conductivity. Phenomenologically, the efficiency of a thermoelectric material is quantified by the dimensionless figure of merit [4]

$$ZT = \frac{\sigma S^2}{\kappa} T, \tag{1}$$

where σ is the electrical conductivity, S the Seebeck coefficient, κ the thermal conductivity (including both lattice κ_L and electronic κ_e contributions), and T the operating temperature.

Among the most promising candidates in this context are perovskites, which offer very appealing properties. These materials feature a distinctive crystal structure composed of corner-sharing octahedra, leading to very low lattice thermal conductivities. Most studies attribute this behavior to the presence of very short phonon lifetimes, primarily associated with dynamic disorder and tilting modes of the octahedral units [5–9]. On the other hand, many perovskites are semiconductors [10], a property that favors reasonably high Seebeck coefficients and results in negligible electronic contributions to the overall thermal conductivity [11]. Unfortunately, however, their relatively large band gaps often lead to extremely low electrical conductivity [12], because of the lack of free charge carriers. This problem is, indeed, very general affecting halide perovskites as well as other emerging promising candidates displaying intrinsically low lattice thermal conductivities and tunable electronic structures. In particular, it is notable to mention compounds such as half-Heusler alloys [13–15], skutterudites [16–18], clathrates [19–23], and chalcopyrites [24–30], which have long been studied for their

*Contact author: acappai@dsf.unica.it

favorable balance between electrical and thermal transport properties. More specifically, skutterudites show low thermal conductivities [18], below 1 $W\,m^{-1}\,K^{-1}$, while half-Heusler materials display very large Seebeck coefficients and tolerance to disorder [15], leading to ZT possibly reaching values as high as 1.6. These systems, even if exemplify different design paradigms, are still actively investigated to suppress lattice thermal conductivity and increase the free charge carrier concentration.

A natural solution to bypass these limitations, widely and successfully applied in conventional semiconductors for electronic applications, is chemical doping, which can significantly increase the carrier concentration. However, doping is not without drawbacks: The introduction of charged impurities perturbs the crystal lattice, thereby affecting both the phonon and the electron properties. From a thermoelectric perspective, this can have a mixed impact. On one hand, it reduces the lattice thermal conductivity, a beneficial effect for enhancing ZT. On the other hand, it introduces Coulomb scattering, an additional source of electron scattering beyond the intrinsic electron–phonon interaction. This further limits electron lifetimes and, in turn, reduces electrical conductivity. Moreover, at high doping levels, the electronic contribution to the thermal conductivity can no longer be neglected, which in turn reduces the improvements in ZT.

Another interesting approach is instead based on a precise nano-engineering of the material exploiting grain-boundary scattering, i.e., the reduction of carrier and phonon mean free path because of the finite-size of the crystalline regions (the grains), where they can freely propagate. The presence of these nanocrystalline domains, in fact, can effectively generate very distinct mean free paths for charge carriers and phonons, and it is in principle possible to design materials where heat transport is limited while maintaining a fairly reasonable high charge transport, thus resulting in an overall increase of ZT.

In both cases, an accurate assessment of the feasibility of these strategies must take into account the competing effects of several different scattering mechanisms present in the material. In particular, it requires reliable estimates of the scattering rates associated with the dominant processes, namely (i) phonon–phonon, (ii) electron–phonon for pristine materials, (iii) Coulomb scattering (in the presence of charged impurities), and (iv) phonon impurity. Once the carrier lifetimes associated with these processes are known, the Boltzmann transport equation (BTE) provides a rigorous framework for computing the resulting transport coefficients: κ_e, σ, and S for charge carriers and κ_L for phonons.

In two of our previous studies [31,32], we thoroughly investigated the thermal and electronic transport properties of the pristine double halide perovskite $Cs_2NaYbCl_6$. It crystallizes in the cubic $Fm\bar{3}m$ space group, corresponding to the elpasolite prototype ($A_2BB'X_6$) structure. Its lattice is derived from a rock-salt ordering of the B-site cations, where Na and Yb occupy alternating octahedral sites within a three-dimensional network of corner-sharing [$YbCl_6$] and [$NaCl_6$] octahedra. The conventional cubic cell contains 40 atoms, with the following Wyckoff positions: Yb at 4*a* (0, 0, 0), Na at 4*b* (0, 0, 1/2), Cs at 8*c* (1/4, 3/4, 3/4), and Cl at 24*e* (0, 0.257662, 1/2). The primitive cell corresponding lattice parameters are $a = b = c = 7.547$ Å and $\alpha = \beta = \gamma = 60^\circ$ [31]. Interestingly, this highly symmetric configuration ensures isotropic transport behavior [31,32].

Using fully first-principles methods, we have calculated the lattice thermal conductivity via phonon–phonon scattering up to fourth-order anharmonicity, and evaluated the electronic transport coefficients S and σ via electron–phonon scattering, the only relevant intrinsic mechanism in pristine, defect-free crystals. We found that, although hole- and electron-mediated charge transport exhibit significant differences (with the latter showing higher mobilities), the resulting ZT values were consistently and significantly low, well below any practical threshold.

In this work we explore possible avenues to tailor the transport properties of $Cs_2NaYbCl_6$ to the aim of enhancing its ZT; more specifically, we investigate the role of nanostructuring and chemical doping (both *p*-type and *n*-type), explicitly including Coulomb scattering from impurities. To this end, we organized the paper as follows: First, in Sec. II, we present the theoretical methods adopted to calculate the impact of charged impurities and grain boundaries on charge carriers and phonons. More specifically, in Sec. II A, we outline the theoretical approach for Coulomb scattering caused by charged impurities, namely the fully *ab initio* calculation based on the EPW code. This allows us to estimate carrier lifetimes as a function of charged impurity number concentration, which we systematically explore in the range 10^{15}–10^{19} cm^{-3}. The choice of these values is motivated by the fact that 10^{13} cm^{-3} concentrations are the typical concentration of native defects in a pristine system (see Ref. [32]), and thus a concentration of 10^{15} cm^{-3} is suitable to describe a low-doping regime. On the other hand, since the upper limit of 10^{19} cm^{-3} is motivated by the need to maintain a dilute regime even at high-doping concentration, as motivated in Sec. II. In Sec. II B, we outline how such impurities impact on thermal transport, using the theoretical framework provided by the Tamura model [33] with the very recent ideas proposed by Snyder *et al.* [34], while in Sec. II C the lifetimes due to grain boundaries are discussed, relying on a very similar theoretical treatment for charge carrier and phonon transport. In Sec. II D, finally, the computational setup adopted is presented.

Our results, presented in Sec. III, provide compelling evidence that Coulomb scattering plays a minor role compared to electron–phonon interactions, which result to be the dominant limiting factor for carrier mobility across the entire doping range, in both *p*- and *n*-type regimes (Sec. III A). Taking this insight into account, we discuss the predicted electrical conductivity and Seebeck coefficient as a function of dopant concentration n_c and temperature (with $T = 300$, 500, and 800 K). The data reveal a clear trade-off: While the Seebeck coefficient decreases with increasing doping, electrical conductivity improves significantly, leading to a marked enhancement of ZT. Interestingly enough, in Sec. III B we show that charged impurities have a limited impact also on thermal lattice conductivity for typical interstitial atom masses. Overall, an increase in ZT is obtained by chemical doping.

In Sec. III C, we show that a similar increase can be very efficiently obtained by nano-engineering, if sufficiently small grain size are chosen. In fact, the calculated reduction of lattice thermal conductivity is significantly larger than the

corresponding decrease of carrier mobilities, revealing a clear asymmetry that can be exploited to raise the ZT value up to $\sim$0.12, compared to 10^{-8} pristine case.

II. METHODS

The transport properties discussed in this work, namely the electrical conductivity σ, the Seebeck coefficient S, and the electronic κ_e and lattice κ_{L} thermal conductivity, are systematically evaluated within the framework of the Boltzmann transport equation (BTE) [35,36]. Within this formalism, the transport coefficients are expressed in terms of the lifetimes of the relevant scattering processes, which dictate the mean free paths of charge carriers and phonons. In all cases considered here, the total scattering rate is obtained by applying Matthiessen rule, whereby the inverse lifetime of each state is given by the sum of the inverse lifetimes associated with the various scattering mechanisms. In the case of charge carrier transport, by considering the Kohn-Sham state labeled by the band index n and the wave-vector $\mathbf{k}$, it can be written as

$$\frac{1}{\tau_{n\mathbf{k}}} = \frac{1}{\tau_{n\mathbf{k}}^{\mathrm{e-ph}}} + \frac{1}{\tau_{n\mathbf{k}}^{\mathrm{imp}}} + \frac{1}{\tau_{n\mathbf{k}}^{\mathrm{gb}}} \tag{2}$$

where, beside the band index n and wave-vector $\mathbf{k}$, the superscripts indicate the specific scattering process: $\tau^{\mathrm{e-ph}}$ is the lifetime due to intrinsic electron-phonon scattering, τ^{imp} the contribution from ionized charged impurities, and τ^{gb} the additional scattering introduced by grain boundaries. We also note that since ionized charged impurity can induce a p- or n-doping regime, it is necessary to label holes and electron lifetimes, which in this paper will be written as τ_h and τ_e, respectively.

The same scheme applies to phonons, with phonon-phonon, phonon-impurity, and phonon-boundary scattering all contributing to the total phonon lifetime. After calculating the lifetimes for each process introduced in Eq. (2), the methodological workflow proceeds in three main steps. First, we evaluate the impact of charged impurities on carrier dynamics by computing the electron–impurity lifetimes. As described in Sec. II A, this is done using the pristine electronic and vibrational structures from Refs. [31,32] and combining them with the intrinsic electron–phonon lifetimes through Matthiessen's rule. The resulting electron and hole lifetimes are then used to solve the BTE and obtain the electrical conductivity, Seebeck coefficient, and electronic thermal conductivity. Second, the effect of dopants on the lattice thermal conductivity is treated by merging the intrinsic phonon–phonon and phonon–impurity lifetimes within the Tamura–Snyder formalism (Sec. II B), which explicitly depends on the dopant mass. Finally, the influence of grain boundaries on both charge carriers and phonons is addressed through the scattering model outlined in Sec. II C. This sequence provides a systematic inclusion of all relevant scattering mechanisms, as schematically summarized in the Introduction and computationally implemented as detailed in Sec. II D.

A. Coulomb scattering: *Ab initio* (Kohn-Luttinger) approach

Scattering from charged impurities is a well-established mechanism limiting carrier mobility in semiconductors, especially at high doping concentrations where it can dominate over intrinsic electron-phonon scattering [37–41]. This mechanism originates from the long-range Coulomb potential generated by ionized dopants: donors, responsible for supplying electrons to the conduction band, and acceptors, for creating holes in the valence band. These charged centers act as long-range scattering sources, reducing carrier lifetimes and mobility.

Historically, the impact of Coulomb scattering has been modeled using semi-phenomenological approaches such as the Brooks-Herring formula [37]. However, a more rigorous and modern approach involves computing Coulomb scattering rates from first principles. In this work, we have made use of the EPW code implementation [41,42], where the impurity potential is modeled in the first Born approximation as a point charge embedded in a dielectric continuum. The potential is periodic over the supercell and includes the static dielectric tensor $\boldsymbol{\varepsilon_0}$ of the host crystal,

$$\phi(\mathbf{r};\mathbf{r}_0) = \frac{4\pi Ze}{\varepsilon_0} \sum_{\mathbf{G}\neq -\mathbf{q}} \frac{e^{i(\mathbf{q}+\mathbf{G})\cdot(\mathbf{r}-\mathbf{r}_0)}}{(\mathbf{q}+\mathbf{G})\cdot\boldsymbol{\varepsilon_0}\cdot(\mathbf{q}+\mathbf{G})}, \tag{3}$$

where $\mathbf{r}_0$ is the impurity position and $\mathbf{G}$ are the reciprocal lattice vectors. The corresponding transition rate between Kohn-Sham states $\psi_{n\mathbf{k}}$ and $\psi_{m\mathbf{k}+\mathbf{q}}$ owing to a distribution of N_{imp} random impurities is obtained after performing a Kohn-Luttinger configurational average [43],

$$\frac{1}{\tau^{\mathrm{imp}}_{n\mathbf{k}\to m\mathbf{k}+\mathbf{q}}} = \frac{2\pi}{\hbar} n_c |g_{mn}(\mathbf{k},\mathbf{q})|^2 \delta(\varepsilon_{n\mathbf{k}} - \varepsilon_{m\mathbf{k}+\mathbf{q}}), \tag{4}$$

with the matrix element

$$g_{mn}(\mathbf{k},\mathbf{q}) = \frac{-e^2}{4\pi\varepsilon_0} \sum_{\mathbf{G}\neq -\mathbf{q}} \frac{\langle u_{m\mathbf{k}+\mathbf{q}} | e^{i\mathbf{G}\cdot\mathbf{r}} | u_{n\mathbf{k}}\rangle}{(\mathbf{q}+\mathbf{G})\cdot\boldsymbol{\varepsilon_0}\cdot(\mathbf{q}+\mathbf{G})}. \tag{5}$$

These matrix elements, with a formal structure very similar to the corresponding electron-phonon g^{ν}_{mn}, effectively account for the dielectric screening, providing a description of the interaction of the point charges with the surrounding crystal environment.

Following Refs. [41,42], the crucial issue of dealing with divergence of the Coulomb potential for $\mathbf{q}\to 0$ is solved by a regularization procedure. Using the physical guess that ionized impurities are screened by the charge carriers they generate, a free-carrier screening is introduced via the Thomas-Fermi approximation, whereby the dielectric function becomes [41,42]

$$\varepsilon_{\mathrm{tot}}(\mathbf{q}) = \varepsilon_0 + \frac{q^2_{\mathrm{TF}}}{q^2}, \tag{6}$$

with q_{TF} the Thomas-Fermi screening wave-vector, computed from the electronic density of states at the Fermi level.

In this work, the impact of charged impurities on the transport coefficients of $Cs_2NaYbCl_6$ is evaluated using the *ab initio* method, which yields scattering rates fully accounting for the material electronic structure.

B. Impurity scattering on phonons: Tamura-Snyder approach

Doping introduces ionized impurities that scatter both charge carriers and phonons, perturbing the translational symmetry of the crystal. This impurity-induced phonon scattering represents a key mechanism limiting lattice thermal conductivity, particularly in materials with significant substitutional, interstitial, and vacancy disorder.

Traditionally, for inorganic semiconductors as Si, Ge, and GaAs, substitutional doping has been the most widely explored strategy for introducing charge carriers. This choice, in fact, is characterized by several advantages: substitutional dopants can be energetically more stable, are easier to incorporate during synthesis, and tend to introduce well-controlled shallow levels in the electronic structure [44–46]. Furthermore, substitutional atoms generally diffuse less than interstitials, enhancing their thermal and chemical stability in typical semiconductors such as GaAs [47].

Nevertheless, interstitial doping is equally possible and has been recently explored in perovskites [48–50], resulting in interstitial dopants to be beneficial in suppressing the migration of halide ions. In perovskites, in fact, interstitials can offer benefits such as enhanced phonon scattering, which can in turn lead to reduction of lattice thermal conductivity and increase in ZT [51]. In this respect, if compared to covalent semiconductors, the peculiar lattice of halide perovskites is more suitable for hosting interstitial defects, because of the presence of large interstitials cavities between the octhaedral units. Also, the overall lower lattice stiffness allows the inclusion of interstitials with relatively low lattice distortions [52].

In any case, because of the dominant presence of substitutional defects in literature compared to interstitials, theoretical models have rarely addressed the specific direct calculation of electron-impurity lifetime for interstitials and vacancies, focusing instead on modeling the effect of substitutional defects. For this case, a widely used analytical framework is the perturbative approach developed by Tamura [33], which describes mass-difference scattering in the harmonic approximation. While this approach is typically applied to isotope scattering, it has been successfully extended to treat dilute concentrations of point defects in various semiconductors and thermoelectric materials [53,54]. In this model, the inverse lifetime $\tau^{\text{imp}}_{\boldsymbol{q},j}(\omega)$ arising from mass disorder for a mode indexed by wave-vector $\boldsymbol{q}$, branch j, and frequency ω is given by

$$\frac{1}{\tau^{\text{imp}}_{\boldsymbol{q}j}(\omega)} = \frac{\pi}{2N_q}\omega^2_{\boldsymbol{q}j}\sum_{\boldsymbol{q}'j'}\delta(\omega-\omega_{\boldsymbol{q}'j'}) \times \sum_{\kappa}\Gamma(\kappa)\left|\boldsymbol{e}^*(\kappa;\boldsymbol{q}'j')\cdot\boldsymbol{e}(\kappa;\boldsymbol{q}j)\right|^2, \quad (7)$$

where N_q is the number of $\boldsymbol{q}$ points in the Brillouin zone, $\omega_{\boldsymbol{q}j}$ is the phonon frequency, and $\boldsymbol{e}(\kappa;\boldsymbol{q}j)$ is the eigenvector (polarization) of atom κ in mode $(\boldsymbol{q}, j)$. The isofactor $\Gamma(\kappa)$ quantifies the mass variance on sublattice κ,

$$\Gamma(\kappa) = \sum_i f_i^{\kappa}\left(1-\frac{m_i^{\kappa}}{\bar{m}_{\kappa}}\right)^2 \quad (8)$$

with f_i^{κ} the fractional concentration of isotope (or dopant) i, m_i^{κ} its mass, and $\bar{m}_{\kappa}$ the average atomic mass on site κ.

Notably, while this model is well suited for substitutional doping (where atomic mass is perturbed but bonding is assumed constant), it was recently suggested [34] its generalization to the case of interstitials or vacancies, which alter both mass and local force constants. In fact, to address this issue, Snyder *et al.* [34] introduced a virial-corrected mass perturbation model that extends the Tamura formalism to non-substitutional defects, allowing to treat them in the framework of the *mass-defect* formalism. To further clarify the physical origin of phonon–defect scattering, we recall the extended formulation introduced by Snyder and coworkers in Ref. [34]. Their analysis revisits the classic treatment of point defects proposed by Klemens [55,56], with Tamura formulation [33] providing a refined approach that preserves the same conceptual foundations. In this framework, the energy perturbation H' induced by a point defect at site $\mathbf{r}$, with a set of nearest-neighbor vectors $\{\mathbf{b}_n\}$, can be written in terms of the atomic displacement vector $\mathbf{u}(\mathbf{r})$ as

$$H' = \frac{1}{2}\Delta M\left(\frac{d\,\mathbf{u}(\mathbf{r})}{dt}\right)^2 + \sum_n \frac{1}{2}\Delta K_{\mathbf{b}_n}[\mathbf{u}(\mathbf{r})-\mathbf{u}(\mathbf{r}-\mathbf{b}_n)]^2 + \sum_n \gamma\,\eta[\mathbf{u}(\mathbf{r})-\mathbf{u}(\mathbf{r}-\mathbf{b}_n)]^2. \quad (9)$$

Here, three distinct contributions are taken into account: a kinetic term arising from the local mass change ΔM, a potential term associated with the variation in the interatomic force constants $\Delta K_{\mathbf{b}_n}$, and an additional potential term stemming from the local strain η induced by a change in atomic radius upon defect insertion, proportional to the γ Grüneisen parameter.

In most practical cases, the strain-induced correction (the third term) is small and is typically considered a third-order effect because of its proportionality to the Grüneisen parameter. This approximation is also plausible for interstitial of perovskite owing to the large interstitial regions between octahedra, which can host relatively large cations without significant distortions. It can therefore be neglected without significant loss of accuracy. The second term, involving changes in interatomic force constants $\Delta K_{\mathbf{b}_n}$, would ideally require explicit DFT calculations on large supercells to quantify, which is often computationally prohibitive.

To bypass this problem, in Ref. [34] it is observed that the remaining Hamiltonian, once the strain term is discarded, is quadratic in the displacement field $\mathbf{u}(\mathbf{r})$. This allows one to exploit the virial theorem, which states that the time-averaged kinetic and potential energies are equal in magnitude. Consequently, the combined effect of mass and bond stiffness variations can be captured by considering only an effective mass perturbation, effectively bypassing the need to explicitly calculate ΔK.

Following this reasoning, the treatment of vacancy defects, as first proposed in Ref. [57], can be recast within the same formalism. In this case, the removal of an atom results in both the loss of its kinetic energy and of the potential energy associated with its chemical bonding. The result is a net loss in potential energy that is approximately twice the average per-atom bonding contribution [34,57]. This motivates the use of an effective mass defect of $m_i^{\kappa} = -M_{\text{host}} - 2\bar{M}$ in Eq. (8), where M_{host} is the mass of the missing atom and $\bar{M}$ is the average atomic mass of the lattice.

Similarly, interstitials are modeled with the use of an effective mass perturbation of $m_i^\kappa = M_{\text{int}} + 2\bar{M}$, accounting for both the dopant mass and the additional bonding interactions formed with two neighboring atoms of average mass $\bar{M}$. This modified model preserves the analytical simplicity of Tamura expression while enabling a unified treatment of substitutional, interstitial, and vacancy-type scattering by simply adopting the proper value for m_i^κ in Eq. (8).

In this study, we focus on interstitial doping, motivated by the hypothesis that interstitials may enhance phonon scattering more effectively, an effect beneficial for ZT increase. We thus adopted the Snyder-modified Tamura approach to quantify the phonon lifetimes and use the resulting linewidths as input to Boltzmann transport calculations.

C. Grain boundary scattering for charge carriers and phonons

Grain boundaries in polycrystalline materials act as extended structural defects, introducing additional scattering mechanisms for both electrons and phonons. These boundaries typically act as partially reflective interfaces, disrupting coherent transport and reducing carrier lifetimes. This effect is particularly important in nanostructured materials, where the grain size approaches the mean free path of carriers or phonons.

The phonon lifetime $\tau^{\text{gb}}_{\mathbf{q}j}$ for the phonon mode $\mathbf{q}j$ (or, analogously, the carrier lifetime in the electron state $\mathbf{k}n$) in the presence of only grain boundary scattering can be expressed as [36,58]

$$\frac{1}{\tau^{\text{gb}}_{\mathbf{q}j}} = \frac{2|\mathbf{v}_{\mathbf{q}j}|}{L} \tag{10}$$

where $\mathbf{v}_{\mathbf{q}j}$ is the group velocity, and L is the effective grain size. The term captures the additional scattering caused by grain boundaries under the assumption of fully diffusive boundary conditions.

Since $\tau^{\text{gb}}_{\mathbf{q}j}$ and $\tau^{\text{gb}}_{\mathbf{k}n}$ can, in principle, be substantially different, grain boundary scattering offers a valuable way to distinctively reduce thermal and electrical conductivities, an effect exploited in the design of thermoelectric materials with suppressed lattice thermal conductivity.

The inverse dependence on grain size (L) highlights the tunability of transport properties via microstructural engineering. As L decreases, boundary scattering increases, enabling independent control over the mean free paths of carriers and phonons, which, as we will show, is essential for optimizing the thermoelectric figure of merit ZT.

D. Numerical implementation

All first-principles calculations presented in this work were performed using the same computational framework and parameters detailed in Refs. [31,32], which provide a comprehensive description of the adopted pseudopotentials, energy cutoffs, Brillouin zone sampling, and PBE exchange-correlation functional. Here, we briefly summarize the main settings for completeness.

Calculations were carried out using the QUANTUM ESPRESSO suite [59,60], employing ultrasoft scalar-relativistic pseudopotentials, a plane-wave kinetic energy cutoff of 70 Ry, and charge density cutoff of 350 Ry. In this framework, spin–orbit coupling (SOC) is not included through the full relativistic operator but only at the scalar level. Although $Cs_2NaYbCl_6$ contains the heavy element Yb, whose $4f$ electrons could, in principle, introduce spin–orbit and correlation effects, we adopted pseudopotentials with $4f$ electrons frozen in the core, effectively modeling the Yb^{3+} oxidation state. This choice is justified by our previous works [31,32], which demonstrated that explicit treatment of $4f$ states leads to artificial metallicity due to strong correlations, inconsistent with the experimentally observed wide-gap insulating behavior. On the other hand, hybrid functional calculations or DFT + U could in principle recover the correct electronic structure, but the former are computationally prohibitive for this system, and the latter is currently incompatible with the EPW implementation used here. Moreover, spin–orbit corrections were previously shown to produce only minor quantitative changes in the band structure [32]. For these reasons, we are confident that the scalar-relativistic approximation provides a consistent and physically reliable description, without affecting the relative trends in transport properties discussed in this work. The electronic structure was calculated on a $7 \times 7 \times 7$ Monkhorst-Pack $\mathbf{k}$-point mesh for self-consistent field (SCF) calculations, and refined via non-self-consistent field (NSCF) runs on a denser $15 \times 15 \times 15$ grid. Phonon properties were evaluated using density-functional perturbation theory as implemented in the `ph.x` module, using a $7 \times 7 \times 7$ $\mathbf{q}$-point grid. Wannier interpolation of electron and phonon properties was performed using the EPW code [61], with initial projectors chosen as Cl p orbitals for valence states and Cs s orbitals for conduction states. All calculations were performed within the dilute-defect and rigid-band approximations, whereby defects modify carrier and phonon lifetimes without altering the underlying electronic or vibrational structures. Accordingly, the electron and phonon datasets from our previous works [31,32] were used as reference. The doping process was not modeled through explicit supercell calculations, but through well-established perturbative formalisms describing scattering by impurities and grain boundaries. Charge carriers, ionized impurity and grain boundary scattering rates were computed *ab initio* within EPW using the pristine DFT band structure, with defect concentration and charge state as input parameters. Phonons and defect scattering rates were in turn evaluated via the Tamura–Snyder formalism implemented in ALAMODE, using fourth-order interatomic force constants from the pristine crystal. Finally, thermal band-gap renormalization was neglected, since $Cs_2NaYbCl_6$ has a wide gap (>3 eV), and temperature-induced shifts are expected to be only a few meV, thus negligible for the present analysis. To ensure consistency across all calculations, the lifetimes τ^{imp} and τ^{gb} for both electrons and phonons were computed using the electronic and vibrational datasets established in Refs. [31,32]. Specifically, the temperature-dependent phonon dispersion relations $\omega_{\mathbf{q}j}(T)$, group velocities $\mathbf{v}_{\mathbf{q}j}(T)$, and intrinsic phonon–phonon scattering times $\tau^{\text{ph}-\text{ph}}_{\mathbf{q}j}$ from Ref. [31] were used as input for calculating the phonon–impurity $\tau^{\text{imp}}_{\mathbf{q}j}(\omega)$ [see Eq. (7)] and grain boundary $\tau^{\text{gb}}_{\mathbf{q}j}$ [see Eq. (10)] relaxation times. These extrinsic phonon lifetimes were then incorporated into the calculation of the lattice thermal conductivity κ_{L} using the ALAMODE package [62,63], which includes higher-order anharmonicity effects.

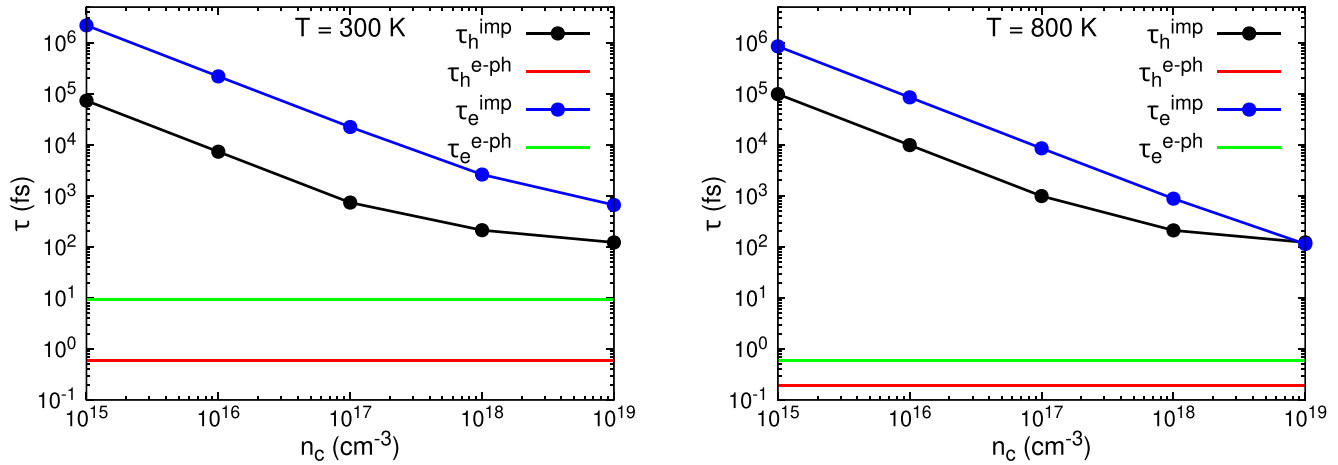

FIG. 1. Hole τ_h and electron τ_e lifetimes in $Cs_2NaYbCl_6$ at $T = 300\,\mathrm{K}$ (left) and $T = 800\,\mathrm{K}$ (right). $\tau_{e,h}^{\mathrm{e-ph}}$ represent lifetimes owing to intrinsic carrier-phonon scattering and are reported as red (holes) and green (electron) lines, while $\tau_{e,h}^{\mathrm{imp}}$ represent lifetimes owing solely to Coulomb scattering from charged impurities (black and blue dots). In the latter case, lines are just a guide for the eye.

The electron–impurity $\tau_{n\mathbf{k}}^{\mathrm{imp}}$ and electron grain boundary $\tau_{n\mathbf{k}}^{\mathrm{gb}}$ lifetimes were evaluated starting from the band structure reported in Ref. [32]. The EPW code was used to solve the Boltzmann transport equation in the presence of Coulomb impurity scattering [41] and grain boundary scattering [42] within the iterative scheme, yielding temperature- and doping-dependent carrier mobilities and relaxation times.

The Seebeck coefficient S and the electronic contribution to the thermal conductivity κ_e were computed using the BOLTZTRAP2 code [64], adopting the rigid-band approximation and including doping effects through a shift in the chemical potential μ. To ensure accurate evaluation of κ_e, an average relaxation time was extracted from the detailed, energy-dependent lifetimes obtained using EPW. All transport coefficients were calculated as functions of temperature T, carrier concentration n_c, and grain size L, to assess their influence on the behavior of σ, S, κ_e, and κ_{L}.

Finally, the thermoelectric figure of merit ZT was obtained using Eq. (1), fully including the intrinsic (phonon–phonon and electron–phonon) and extrinsic (impurity and boundary) scattering mechanisms in the determination of each individual transport coefficient.

III. RESULTS AND DISCUSSION

A. Impact of charged impurities on electrical transport coefficients and power factor

Using the first-principles framework implemented in EPW (as detailed in Sec. II A), we computed the typical carrier lifetime associated with electron–charged impurity scattering. The results are reported in Fig. 1, where, for comparison, we also show the lifetimes owing to intrinsic electron–phonon scattering, as previously determined in our earlier work [32]. We remark that in Fig. 1 the intrinsic scattering lifetime results independent of the dopant concentration since it accounts for an intrinsic process always present in the material. All data were obtained at two representative temperatures, $T = 300\,\mathrm{K}$ (Fig. 1, left) and $T = 800\,\mathrm{K}$ (Fig. 1, right), spanning the operational window for potential thermoelectric applications of the material. It is evident that in $Cs_2NaYbCl_6$, the dominant scattering mechanism governing charge carrier mobility is intrinsic electron–phonon interaction. Even for the highest investigated dopant concentration, impurity scattering yields systematically longer carrier lifetimes. We interpret the observed trend as a consequence of a weak influence of impurity scattering caused by the minor perturbing effect of the charged impurity on crystal potential, as well as the intrinsic strong activation of all electron–phonon scattering channels even at $T = 300\,\mathrm{K}$.

Regarding the first point, we argue that the relatively large dielectric constant of the material, computed via linear-response theory as $\varepsilon_r = 9.3$, leads to substantial dielectric screening of the Coulomb potential induced by the impurities, thereby reducing their impact on scattering. As for the second point, our previous work already highlighted the presence of numerous optical phonon modes with large electron–phonon matrix elements g_{mn}^{ν} even at room-temperature, resulting in frequent scattering events.

Additionally, Fig. 1 shows that electron–impurity scattering lifetimes are consistently longer than those for hole–impurity scattering across both low and high temperatures. In our understanding, this trend is naturally explained by the lower effective mass of electrons compared to holes, specifically $m_e^* = 1.7$ and $m_h^* = 2.7$ (in electron mass units). Since the carrier lifetime scales inversely with the square root of the effective mass, this behavior directly reflects the specific band structure of $Cs_2NaYbCl_6$.

The same analytic framework also explains the observed increase in lifetime with temperature. At higher temperatures, the Debye screening length increases, which physically corresponds to a weakening of impurity scattering because of enhanced screening. Thus, the impact of impurity scattering on charge transport becomes even less significant as temperature rises. As observed in Ref. [32], we argue that the weaker temperature dependence observed for p-type transport arises from the more localized character of the valence-band states, whereas the higher mobility and stronger temperature sensitivity of n-type transport reflect the greater delocalization of conduction-band carriers.

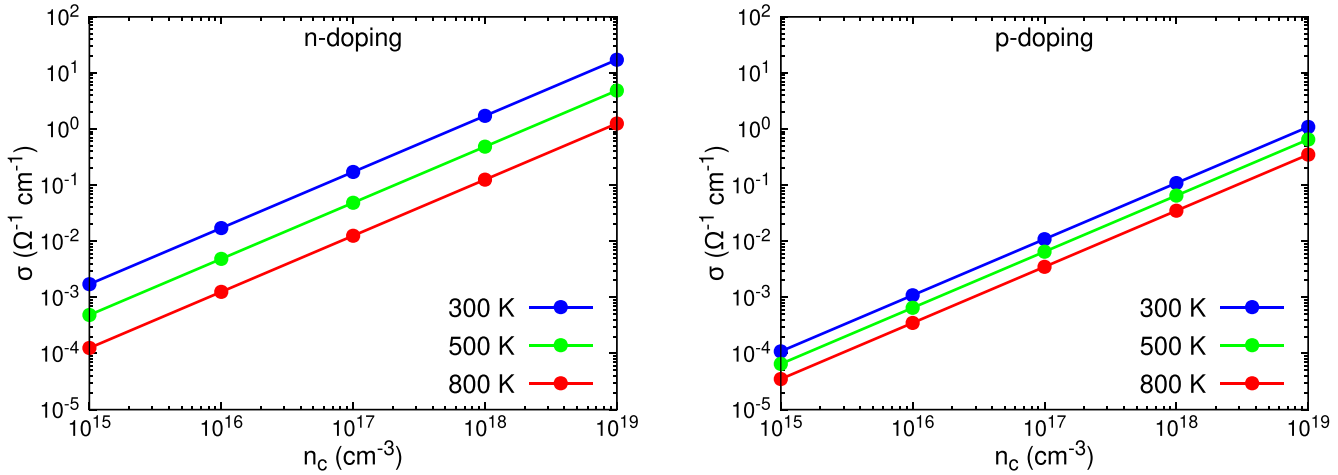

FIG. 2. Electrical conductivity σ as a function of carrier number density n_c in the case of n- (left) and p-type (right) doping. Blue, green, and red points indicate the three different temperatures investigated (300, 500, and 800 K, respectively).

These considerations lead to the conclusion that intrinsic mechanisms dominate over extrinsic (impurity-related) scattering, a finding that carries conceptual importance. As noted in the Introduction, charged impurity doping affects the material in two opposing ways: it increases the carrier concentration (enhancing conductivity) but also introduces additional scattering channels (which reduce mobility). However, if impurity-induced scattering times are sufficiently long, the adverse effect becomes negligible, and only the beneficial increase in carrier concentration remains, resulting in an overall enhancement of electrical conductivity. To quantify this effect, Fig. 2 displays the electrical conductivity σ as a function of charged impurity concentration n_c, including the total relaxation time from both electron–phonon and impurity scattering. Results are shown for electrons and holes (Fig. 2, left and Fig. 2, right, respectively) at three representative temperatures (300 K, 500 K, and 800 K) corresponding to low-, mid-, and high-temperature thermoelectric regimes. We observe that, although higher temperatures reduce conductivity, increasing the concentration of donor or acceptor impurities leads to a substantial improvement. This behavior is consistent with the dominant role of intrinsic mobility, which, as already established in Ref. [32], decreases with temperature, thus reducing conductivity.

A very different trend is obtained for the Seebeck coefficients. Figure 3 shows that increasing the dopant concentration (both for n- and p-type doping in left and right panel, respectively) consistently leads to a reduction in the magnitude of the Seebeck coefficient, opposite to the trend observed for electrical conductivity. This behavior, often reported in the literature for semiconductors [36,65], is typically explained, in the context of the Boltzmann transport equation under the relaxation time approximation (RTA), by defining the transport function $\Sigma(E,T)$ [64],

$$\Sigma(E,T) = \int \sum_n \mathbf{v}_{n,\mathbf{k}} \otimes \mathbf{v}_{n,\mathbf{k}} \tau_{n,\mathbf{k}} \delta(E - E_{n,\mathbf{k}}) \frac{d\mathbf{k}}{8\pi^3}, \quad (11)$$

where E is the carrier energy and $\mathbf{v}_{n,\mathbf{k}}$ and $\tau_{n,\mathbf{k}}$ are its velocity and lifetime in the nth band at $\mathbf{k}$ wavevector, we have that the Seebeck coefficient can be expressed as [64]

$$S(T) = \frac{1}{qT} \frac{\int \Sigma(E,T)(E-\mu)\partial_E f^0(E,\mu,T)dE}{\int \Sigma(E,T)\partial_E f^0(E,\mu,T)dE} \quad (12)$$

where μ is the chemical potential (shifted accordingly to the doping concentration) while $\partial_E f^0(E,\mu,T)$ is the short-hand notation for the derivative of the Fermi-Dirac equilibrium distribution function respect to the energy.

Focusing on the numerator of Eq. (12), it is evident that the Seebeck coefficient results large only when the chemical potential μ is sufficiently far from the band edges, a condition quantified by the $(E-\mu)$ term in the integral. Doping, on the other hand, shifts μ closer to the conduction or valence band, thereby reducing the integrand and hence S. Comparing the two doping regimes, we find similar magnitudes for electrons and holes, although electron transport exhibits a stronger temperature dependence. In both cases, S increases with temperature, primarily because of the temperature-induced broadening of the Fermi–Dirac derivative $\partial_E f^0(E,\mu,T)$, which increases the number of carriers contributing to S. However, the more limited increase in the hole case likely originates from the higher degree of spatial localization of valence band states, compared to the more delocalized conduction band states.

Combining these results for σ and S, we compute the power factor, $\mathrm{PF} = \sigma S^2$, shown in Fig. 4 as a function of carriers concentration for both transport regimes across different temperatures. In both doping scenarios, the PF increases with dopant density but decreases with temperature. This trend underscores the dominant role of electrical conductivity in shaping the power factor, while the variations in the Seebeck coefficient play a less relevant role. Moreover, the stronger temperature dependence of PF in the electron-doped case again reflects the delocalized nature and band topology of conduction states in $Cs_2NaYbCl_6$.

To complete our analysis of the effect of doping on electronic transport, we report in Fig. 5 the electronic contribution to the thermal conductivity κ_e. Even at the highest dopant concentrations considered, κ_e remains well below both the experimentally measured total thermal conductivity and our

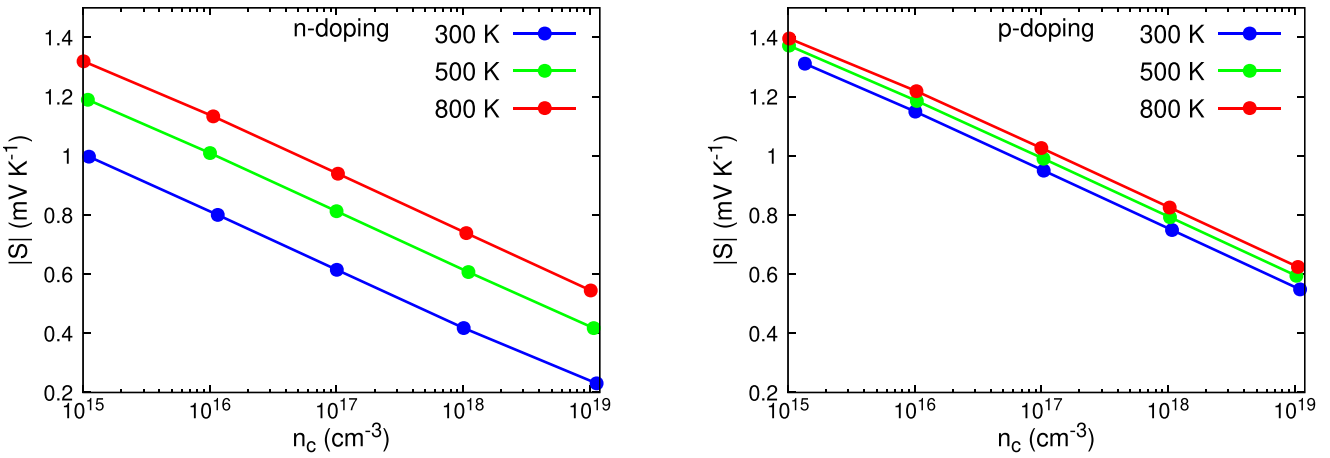

FIG. 3. Seebeck coefficients S as a function of carrier number density n_c in the case of n- (left) and p- (right) doping. Blue, green, and red points indicate the three different temperatures investigated (300, 500, and 800 K, respectively).

previously reported theoretical estimates for the pristine system ($\simeq$0.51Wm^{-1}K^{-1} [31,32]). This confirms that, likely because of the wide band gap of $Cs_2NaYbCl_6$ (5.3 eV), the electronic contribution is negligible compared to the lattice thermal conductivity.

As expected, we note a distinct behavior of κ_e with temperature T, decreasing monotonically with T for both electrons and holes. This trend is a direct consequence of the reduction in $\tau_{n\mathbf{k}}$, driven by the enhanced rate of intrinsic electron–phonon scattering. In fact, if the relaxation were temperature-independent, κ_e would be expected to increase monotonically with temperature owing to the larger number of thermally activated carriers.

To assess the full impact of these contributions on the total thermal conductivity; however, it is necessary to evaluate the lattice component κ_L as a function of impurity concentration, a task we address in the following subsection.

B. Impact of dopants on lattice thermal conductivity

To complete our analysis of the doping strategies affecting the thermoelectric performance of $Cs_2NaYbCl_6$, we now turn to the impact of defects on the lattice thermal conductivity, focusing specifically on phonon–impurity scattering. As outlined in Sec. II B, the model developed by Tamura [33] provides a convenient framework for estimating the phonon–impurity lifetime in the presence of substitutional disorder. Within this approach, scattering rates are governed by the isofactor Γ [see Eq. (8)], which, using the mass variance on each sublattice site, dictates the lifetime magnitude.

However, given that Tamura's theory assumes minimal lattice distortion, we restricted our analysis to substitutional dopants that preserve the host crystal structure. Based on comparisons of ionic radii, we identified barium, zirconium, and cesium as suitable candidates when substituted at the sites listed in Table I, enabling p-type (Ba) and n-type (Zr, Cs) doping, respectively. The corresponding isofactors, computed for a nominal dopant concentration of $n_c = 10^{19}$ cm^{-3}, are also reported in the final column of Table I. While a comprehensive thermodynamical evaluation of defect energy formation is still missing, a recent work [66] showed that in the case of vacancies even higher concentrations have reasonable formation energies (always less than 0.5 eV) if n_c does

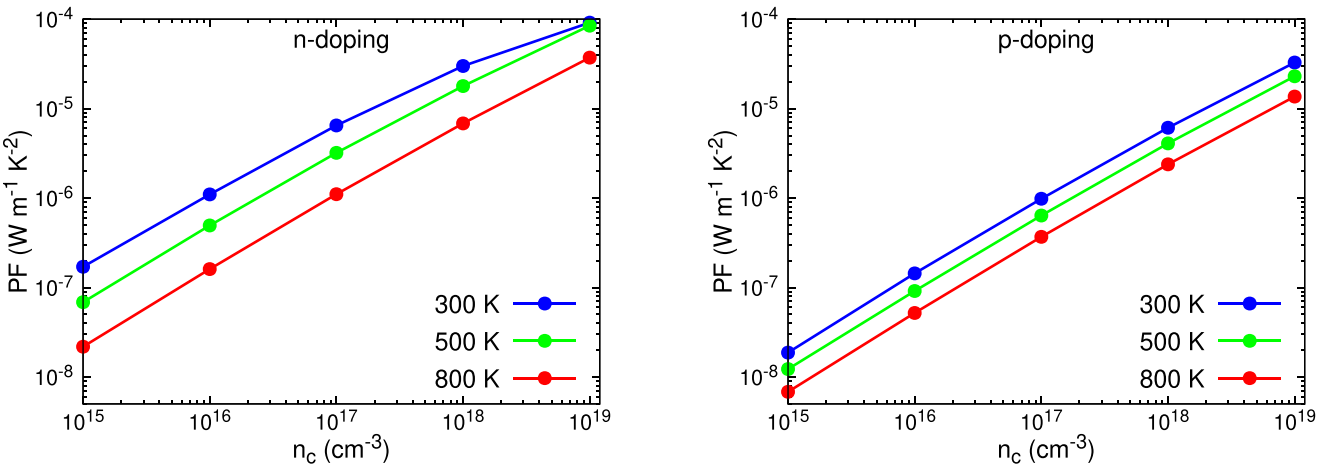

FIG. 4. Power factor PF $= \sigma S^2$ as a function of carrier number density n_c in the case of n- (left) and p-type (right) doping. Blue, green, and red points indicate the three different temperatures investigated (300, 500, and 800 K, respectively).

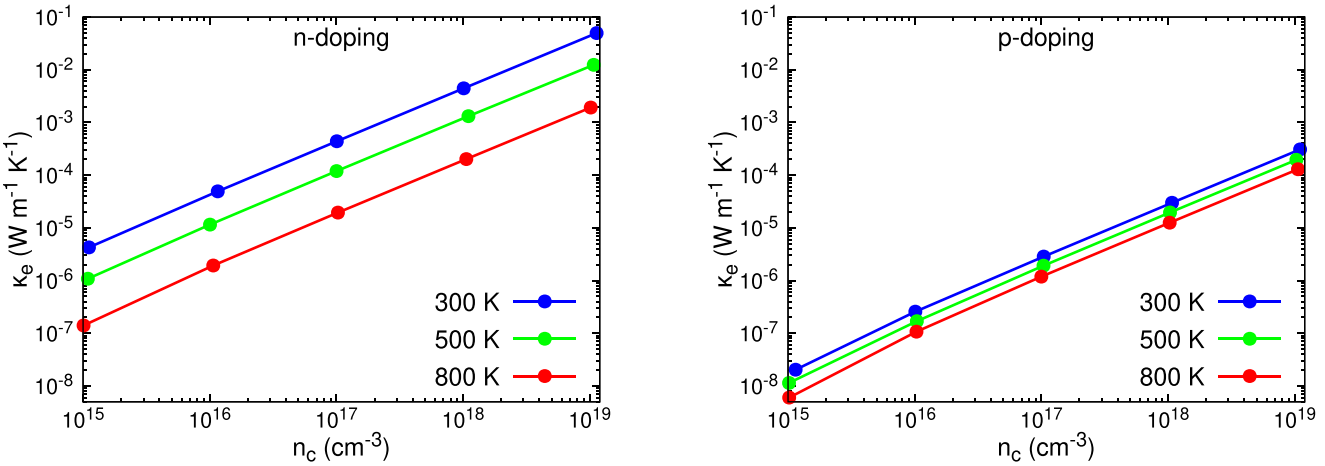

FIG. 5. Electronic contribution to thermal conductivity κ_e as a function of carrier number density n_c in the case of n- (left) and p-type (right) doping. Blue, green, and red points indicate the three different temperatures investigated (300, 500, and 800 K, respectively).

not exceed 10^{21} cm^{-3}, thus providing a reason of plausibility for our guess. Also, it is reported in literature that inclusion of atoms, as terbium and similar atomic species, is experimentally feasible [48–50,67], strongly supporting our hypothesis.

To treat defects that lie beyond the validity of Tamura formalism (such as interstitials and vacancies) we employed the extended approach proposed in Ref. [34], as outlined in Sec. II C. This method allows the effect of these defects to be incorporated within a modified version of the isofactor, by redefining the mass perturbation using a virial-theorem-based argument. In this approximation, the net impact of an interstitial or vacancy is represented as an effective mass modification on the host site, thus preserving the harmonic treatment of the lattice dynamics.

It is important to remark that this approximation is very useful to keep the resulting computational workload lower, as a direct *ab initio* evaluation of the impact of defects at realistic concentrations is prohibitively expensive. Even in heavily doped regimes (as with one defect per $\sim 10^4$ host atoms) modeling such concentrations would require extremely large supercells, making standard lattice dynamics approaches almost impossible. Additionally, the lack of translational symmetry in defective systems does not allow to exploit symmetry operations to reduce the number of displacement configurations needed for force constant extraction. The limitation of the model, however, is because of the assumption that defects have not altered phonon spectrum compared to the pristine case, which, however, is reasonable in the dilute case.

Accordingly, in the remainder of our analysis, we retain a dopant concentration of $n_c = 10^{19}$ cm^{-3}, a regime where the phonon eigenfrequencies and intrinsic lifetimes are expected to remain largely unperturbed by atomic insertion or removal. For the interstitials, we focused on dopants inducing either p-type or n-type doping, consistent with the two charge transport regimes presented in Sec. III A. As dopant chemical species we select atoms on the base of their ability to occupy interstitial sites without introducing substantial lattice deformation. To achieve this, after pristine structure structural relaxation, we identified the cavity formed between neighboring octahedra, centered on Cs atoms, as the most favorable interstitial site. This void features an effective radius of $\sim$3.8 Å, large enough to accommodate small cations (e.g., Na, K) and anions (e.g., Cl), which serve as proxies for hole and electron doping, respectively. In our calculations, and in the spirit of Ref. [34], the corresponding effective defect mass were assigned to Cs sites.

For vacancy defects, we considered the absence of each of the four atomic species in the host lattice and computed their individual contributions to phonon–impurity scattering. The resulting isofactors for both interstitials and vacancies are listed in Tables II and III, respectively.

Starting with the analysis of interstitial defects, Fig. 6 presents the phonon–impurity scattering lifetimes at $T =$ 300 K for three representative interstitial types (in red, blue,

TABLE I. Mass parameters for substitutional dopants in $Cs_2NaYbCl_6$ at a concentration of 10^{19} cm^{-3}. The dopant replaces the host atom at the specified site. The average mass $\bar{m}$ (expressed in atomic mass units u) at the site includes the contribution of the dopant, and Γ is the resulting isofactor.

Dopant (Subst.)	Site	$\bar{m}$ (u)	Isofactor Γ
Ba	Cs	132.906	3.48×10^{-7}
Zr	Yb	173.028	7.03×10^{-5}
Ca	Yb	173.012	1.86×10^{-4}

TABLE II. Mass parameters for interstitial dopants in $Cs_2NaYbCl_6$ at a concentration of 10^{19} cm^{-3}. The interstitial is added to the host atom at the specified site. The effective mass m_{def} (expressed in atomic mass units u) is calculated using the virial correction, and Γ is the resulting isofactor.

Dopant (Interst.)	Site	m_{def} (u)	Isofactor Γ
Na	Cs	158.83	5.97×10^{-5}
K	Cs	174.94	1.56×10^{-4}
Cl	Cs	171.29	1.31×10^{-4}

TABLE III. Mass parameters for vacancies in $Cs_2NaYbCl_6$ at a concentration of 10^{19} cm^{-3}. The effective mass m_{def} (expressed in atomic mass units u) is calculated using the virial correction, with Γ the resulting isofactor.

Vacancy Type	m_{def} (u)	Isofactor Γ
Cs	−268.75	4.12×10^{-4}
Na	−158.83	3.90×10^{-3}
Yb	−308.89	9.27×10^{-4}
Cl	−171.29	1.79×10^{-2}

and green), and are compared with the intrinsic phonon–phonon scattering lifetimes (in black) previously reported in Ref. [31]. Figure 6 clearly shows that all interstitial types yield comparable results. In each case, the phonon–impurity lifetimes remain significantly longer than their intrinsic phonon–phonon counterparts. As a consequence of Matthiessen rule, the total phonon scattering rate is thus dominated by the intrinsic phonon-phonon contribution, with impurity scattering playing a negligible role under these conditions. This result suggests that intrinsic anharmonicity is already sufficiently strong to bring the system close to its minimal attainable phonon lifetimes. This trend is further confirmed in Fig. 7, where we plot the total phonon lifetimes obtained by combining intrinsic and impurity-induced scattering.

The negligible impact of interstitials is also reflected in the calculated lattice thermal conductivity at $T = 300$ K, shown in Fig. 8. Here, the pristine compound is compared against the three representative interstitial cases.

No sizable change in κ_L is observed upon doping, confirming the minor role played by phonon–impurity scattering in this material. Moreover, recalling that the electronic contribution κ_e remains negligible throughout the studied doping range, we conclude that the total thermal conductivity $\kappa = \kappa_e + \kappa_L$ is entirely dominated by its lattice component κ_L under all relevant conditions.

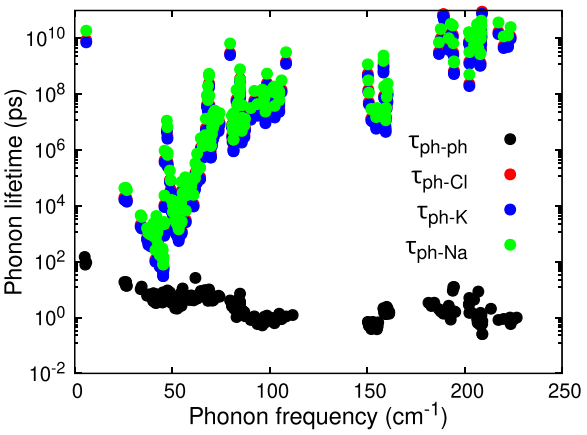

FIG. 6. Phonon lifetimes in pristine and doped $Cs_2NaYbCl_6$ at $T = 300$ K. Black points correspond to intrinsic phonon–phonon lifetimes, while colored points denote phonon–impurity lifetimes for three representative interstitial cases.

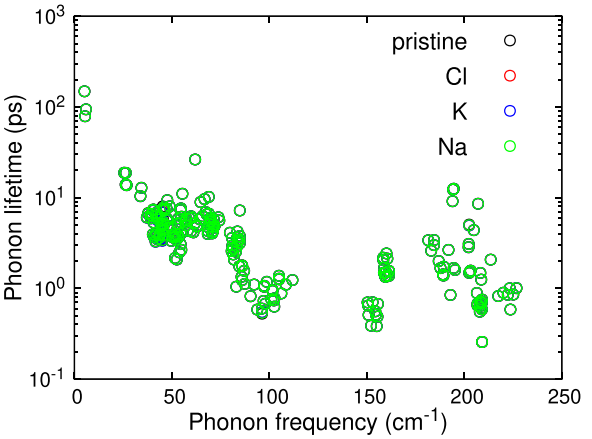

FIG. 7. Total phonon lifetimes in $Cs_2NaYbCl_6$ including both intrinsic phonon–phonon and extrinsic phonon–impurity scattering mechanisms.

Similar results were found for all substitutional defects and for vacancies, with the only exception of Cl vacancies, which result in a reduction of κ_L of about 16%, a rather modest reduction. In reporting this result, we remark again that the adopted phonon–impurity scattering model follows the formalism originally developed by Tamura [33], which treats mass-disorder perturbations in a harmonic crystal.

To finally comment these findings, we must underline that Tamura model assumes elastic and isotropic scattering, which may not fully capture mode-specific interactions, especially when localized vibrational modes arise around heavy or light defects [68]. Nevertheless, for the low concentrations considered here and the absence of strong structural distortions, the approach remains appropriate, and we can overall conclude that our results indicate that phonon–impurity scattering plays a secondary role in limiting κ_L in $Cs_2NaYbCl_6$, and that intrinsic anharmonicity is the dominant mechanism controlling heat transport.

As final note, we can now evaluate the efficiency of introducing ionized impurity as strategy for improving the ZT figure of merit. In fact, we have shown that while PF

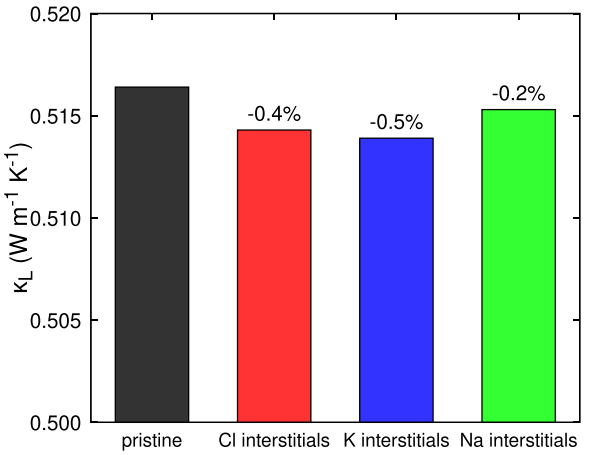

FIG. 8. Lattice thermal conductivity κ_L of $Cs_2NaYbCl_6$ at $T = 300$ K for pristine and interstitially doped cases.

TABLE IV. Electron mobility μ (in $\mathrm{cm^2\,V^{-1}\,s^{-1}}$) as a function of temperature and grain size. The pristine column reports values limited by phonon scattering only.

T (K)	Pristine	$L = 100$ nm	$L = 50$ nm	$L = 10$ nm
300	7.76	11720	5860	1172
500	2.47	8835	4418	884
800	0.78	5741	2870	574

TABLE V. Lattice thermal conductivity κ_L (in $\mathrm{W\,m^{-1}\,K^{-1}}$) as a function of temperature and grain size. The pristine column reports values limited by phonon-phonon scattering only.

T (K)	Pristine	$L = 100$ nm	$L = 50$ nm	$L = 10$ nm
300	0.52	0.41	0.35	0.20
500	0.46	0.39	0.34	0.20
800	0.54	0.46	0.41	0.24

significantly increases, lattice thermal conductivity is almost unaffected. We thus estimate that the highest value of ZT is reached for $T = 300\,\mathrm{K}$ in the n-doping regime at the highest $n_c = 10^{19}\ \mathrm{cm^{-3}}$ ionized impurity concentration: using the PF values calculated and adding the electronic contribution κ_e to the lattice thermal conductivity κ_L, a value of $ZT = 0.052$ is obtained, well above the intrinsic value of $\simeq 10^{-8}$ previously found for the pristine system [32].

C. Impact of grain boundary scattering on thermal and carrier transport

We now turn to the role of grain boundary (GB) scattering in determining the thermoelectric performance of $Cs_2NaYbCl_6$. Here, we explicitly evaluate its effects on both carrier mobility and lattice thermal conductivity by considering representative grain sizes of 100 nm, 50 nm, and 10 nm. These values encompass typical ranges found in experimental polycrystalline samples of halide perovskites and related wide-gap materials [69,70].

In order to analyze the impact on carrier mobility, Table IV reports the calculated electron mobility μ as a function of temperature and grain size. For reference, the intrinsic (phonon-limited) mobility at 300 K is computed to be $\mu_\mathrm{ph} = 7.76\ \mathrm{cm^2\,V^{-1}\,s^{-1}}$, decreasing monotonically with temperature owing to enhanced electron-phonon scattering. When considering grain boundary scattering alone, the computed mobilities are found to be markedly higher than the intrinsic values across the entire temperature range. For instance, at 300 K, the mobility limited solely by 100 nm grains exceeds $1 \times 10^4\ \mathrm{cm^2\,V^{-1}\,s^{-1}}$, reducing to $1.17 \times 10^3\ \mathrm{cm^2\,V^{-1}\,s^{-1}}$ for grains of 10 nm. This behavior is consistent with a simple kinetic picture in which mobility scales linearly with the mean free path, and with grain boundaries imposing an effective upper limit of $L/2$ on the latter. Given the approximate unit cell size of ∼40 Bohr (∼2.1 nm), even the smallest grain size considered here remains several times larger than the characteristic phonon or carrier wavelengths, validating the semiclassical treatment of GB scattering in the Boltzmann framework.

Critically, when both phonon and GB scattering are present, Matthiessen rule dictates that the total mobility is dominated by the smaller of the two scattering rates. Since μ_ph is already limited to values below $1\ \mathrm{cm^2\,V^{-1}\,s^{-1}}$ at elevated temperatures, while μ_GB remains orders of magnitude higher even for 10 nm grains, we conclude that grain boundary scattering plays a negligible role in further reducing mobility in this material. This outcome reflects the inherently poor carrier mobility of $Cs_2NaYbCl_6$, which is already severely limited by strong electron-phonon interactions in the pristine structure. When the impact on lattice thermal conductivity is, instead, analyzed, a striking difference emerges. In fact, grain boundary scattering plays a more marked effect on phonon-mediated heat transport, as shown in Table V. At room temperature, the lattice thermal conductivity decreases from its pristine value of $0.52\ \mathrm{W\,m^{-1}\,K^{-1}}$ to $0.41\ \mathrm{W\,m^{-1}\,K^{-1}}$ and $0.35\ \mathrm{W\,m^{-1}\,K^{-1}}$ for 100 nm and 50 nm grains, respectively. For 10 nm grains, κ_L is nearly halved to $0.20\ \mathrm{W\,m^{-1}\,K^{-1}}$. Similar reductions persist at elevated temperatures, though the relative impact diminishes slightly as intrinsic phonon-phonon scattering strengthens.

This behavior aligns with expectations for polycrystalline systems in which boundary scattering imposes an upper limit on the phonon mean free path, particularly for long-wavelength acoustic modes that dominate thermal transport in this material [38]. The observed κ_L values remain within the typical range reported for halide perovskites with comparable microstructural features, as for example the values calculated by Pandey *et al.* [71].

By combining the two evidences, our analysis reveals that grain boundary scattering has a negligible impact on carrier mobility in $Cs_2NaYbCl_6$, given the already low intrinsic mobilities dictated by electron-phonon interactions. Conversely, its effect on lattice thermal conductivity is more significant, particularly for nanoscale grains, though even in the most extreme case of 10 nm grains the reduction does not exceed 60% compared to the pristine crystal. This outcome suggests that strategies aimed at reducing κ_L via nanostructuring would yield diminishing returns for this class of materials, especially considering the already low thermal conductivities inherent to the class of perovskites [71,72].

In the case in which only nanostructuration strategy is applied to improve ZT, we thus found that the highest attainable values of ZT is obtained in the case of electron mediated transport (assuming the intrinsic carrier density n_c for pristine system [32]) and a grain boundary size of 10 nm. Since σ, S, and κ_e are unaffected while κ_L is reduced to one half of its pristine value, $ZT \simeq 3 \times 10^{-8}$, still significantly low because of the scarcity of carriers (ultimately caused by the high band gap value).

D. Chemical doping and nanostructuration combined impact on *ZT*

To conclude our analysis of strategies aimed at enhancing the thermoelectric figure of merit ZT in $Cs_2NaYbCl_6$, we summarize the key findings obtained from the separate evaluation of chemical doping and nanostructuring effects.

Across all cases investigated, we confirm that one of the principal results established for the pristine system

remains valid [31,32]: Electron-mediated transport exhibits consistently higher mobility than hole-mediated transport. Consequently, *n*-type doping emerges as the most promising strategy to improve the material's thermoelectric performance. Under optimal doping conditions (specifically, a carrier concentration of $n_c = 10^{19}$ cm^{-3} and temperature $T =$ 300 K) the power factor reaches its maximum value, while the lattice thermal conductivity remains essentially unaffected by the introduction of interstitial defects. Furthermore, the electronic contribution to the thermal conductivity κ_e remains negligible, on the order of $\simeq 0.05$ W m^{-1} K^{-1}.

Building on this optimized doping configuration, we examined the additional effect of nanostructuring by imposing a grain size of 10 nm. Our results indicate that the electronic transport properties (i.e., the power factor and κ_e) remain essentially unchanged under this condition. However, the lattice thermal conductivity κ_L is significantly reduced, dropping from approximately 0.52 W m^{-1} K^{-1} to 0.2 W m^{-1} K^{-1} as a direct consequence of enhanced phonon boundary scattering.

By combining these effects, we estimate the highest achievable figure of merit ZT for $Cs_2NaYbCl_6$ to be approximately 0.12 under simultaneous *n*-type doping ($n_c = 10^{19}$ cm^{-3}) and nanostructuring (grain size of 10 nm). This value represents an improvement of several orders of magnitude compared to the pristine system, where ZT was found to be on the order of 10^{-8}. We emphasize, however, that while both strategies contribute to this enhancement, doping plays the predominant role. The reduction in κ_{L} from nanostructuring alone would not suffice to produce such a significant increase in ZT without the concurrent rise in electrical conductivity afforded by doping.

These findings support the hypothesis previously advanced in Ref. [32], namely that the poor thermoelectric performance of pristine $Cs_2NaYbCl_6$ stems primarily from its large band gap and the resulting scarcity of intrinsic carriers. Once this limitation is addressed through carrier injection, the material's performance can be substantially improved. Although the absolute value of $ZT \simeq 0.12$ remains modest, the methodology demonstrated here could be effectively applied to more promising candidates, where starting from a higher intrinsic ZT could lead to competitive thermoelectric materials.

IV. CONCLUSIONS

This work provides a comprehensive, first-principles assessment of thermoelectric transport in the double halide perovskite $Cs_2NaYbCl_6$, a wide-band-gap, lead-free material of growing interest for energy applications. We systematically explored the effects of chemical doping and nanostructuring, two key extrinsic strategies widely employed to optimize thermoelectric performance, in the context of a material whose intrinsic properties are far from optimal. Our goal was twofold: First, to evaluate whether these strategies can meaningfully enhance the figure of merit ZT; second, to clarify the microscopic mechanisms by which they affect the sensible balance between electrical and thermal transport.

Our analysis, grounded in fully *ab initio* methods and employing the Boltzmann transport formalism, incorporates all relevant scattering mechanisms affecting charge carriers and phonons. Specifically, we account for intrinsic interactions such as electron–phonon and phonon–phonon scattering, as well as extrinsic processes including Coulomb scattering from charged dopants, phonon–impurity scattering, and grain boundary effects. This allows us to provide a predictive, material-specific picture of transport in doped and nanostructured $Cs_2NaYbCl_6$.

Our first key finding concerns the role of chemical doping. While the pristine compound suffers from extremely low electrical conductivity because of its large band gap and low intrinsic carrier density, we demonstrate that extrinsic doping (both *n*- and *p*-type) can substantially increase the number of free carriers. Interestingly, we find that Coulomb scattering induced by ionized impurities is strongly screened, owing to a relatively high static dielectric constant ($\varepsilon_r = 9.3$), and is thus negligible compared to intrinsic electron-phonon interactions across a broad range of dopant concentrations (10^{15}–10^{19} cm^{-3}). This insight is crucial since it implies that doping enhances electrical conductivity without introducing significant mobility degradation, thereby enabling a net improvement in the power factor PF.

We also found that the monotonic reduction in the Seebeck coefficient, because of the Fermi level shifting closer to the band edges, for increasing doping levels still assures a sizable increase in the power factor, especially in the *n*-type regime, where electron mobilities are higher owing to the lighter effective mass. Moreover, we verified that the electronic contribution to thermal conductivity κ_e remains small even at high doping levels, a feature beneficial for achieving high ZT values.

The second issue of our investigation focused on nanostructuring, which we modeled via grain boundary scattering, assuming grain sizes ranging from 100 nm to 10 nm. Here, our findings reveal a contrasting effect. While grain boundaries have negligible influence on carrier mobility (again because of the dominant role of electron–phonon scattering) they do significantly affect phonon transport. In particular, grain boundary scattering effectively limits the mean free path of long-wavelength acoustic phonons, which are the main contributors to lattice thermal conductivity κ_{L} in halide perovskites. As a result, κ_{L} is reduced by up to 60% in the most extreme nanostructured case (10 nm grains), falling from 0.52 W m^{-1} K^{-1} to 0.2 W m^{-1} K^{-1} at room temperature.

Interestingly, phonon–impurity scattering, treated via the Tamura–Snyder formalism, was found to play a minimal role. Even at relatively high dopant concentrations, mass-disorder effects introduced by interstitial or vacancy-type defects do not meaningfully impact phonon lifetimes compared to the dominant intrinsic phonon–phonon interactions. This observation further underscores the importance of grain boundary scattering as the principal extrinsic mechanism for κ_{L} reduction.

By combining these effects, we estimate the highest achievable figure of merit ZT for $Cs_2NaYbCl_6$ to be approximately 0.12 under simultaneous *n*-type doping (carrier density of 10^{19} cm^{-3}) and nanostructuring (grain size of 10 nm). This value represents an improvement of several orders of magnitude compared to the pristine system, where ZT was found to be on the order of 10^{-8}. We emphasize, however,

that while both strategies contribute to this enhancement, doping plays the predominant role. The reduction in κ_L from nanostructuring alone would not suffice to produce such a significant increase in ZT without the concurrent rise in electrical conductivity afforded by doping.

These conclusions support the hypothesis previously advanced in Ref. [32], namely that the poor thermoelectric performance of the pristine material stems primarily from its large band gap and the resulting scarcity of intrinsic carriers. Once this limitation is addressed through carrier injection, the material performance can be substantially improved. Even if the predicted figure of merit, $ZT \simeq 0.12$ at 800 K, for $Cs_2NaYbCl_6$ is not large compared to state-of-the-art classical thermoelectrics but comparable to values reported for related halide perovskites. Mature thermoelectric systems such as Bi_2Te_3-based alloys, skutterudites ($CoSb_3$), and half-Heusler compounds can exhibit $ZT \approx 1-1.5$ at similar temperatures under optimized doping and nanostructuring conditions [13,73,74]. By contrast, recent experiments and first-principles calculations on lead-free halide perovskites (including $Cs_2AgBiBr_6$, $Cs_2AgInCl_6$, and the vacancy-ordered Cs_2SnI_6) report ZT values between 0.05 and 0.2 in the range 700–900 K [75–80]. Our result therefore places $Cs_2NaYbCl_6$ among the most promising members of the halide-perovskite family from a thermoelectric perspective, especially considering its ultralow lattice thermal conductivity and the potential for further improvement through controlled doping and nanostructuring, as demonstrated experimentally in related systems. Also, we remark that although the absolute value of $ZT \simeq 0.12$ remains modest, the methodology demonstrated here could be effectively applied to more promising candidates, where starting from a higher intrinsic ZT could lead to competitive thermoelectric materials.

Future work could extend this methodology to a broader class of halide perovskites and related wide-band-gap compounds, identifying optimal candidates where the favorable features of $Cs_2NaYbCl_6$, such as low κ_L, are combined with intrinsically better electronic transport properties.

ACKNOWLEDGMENTS

We acknowledge the financial support under the National Recovery and Resilience Plan (NRRP), Mission 4 Component 2 Investment 1.3 (Call for tender No. 341 published on March 13, 2022) by the Italian Ministry of University and Research (MUR) funded by the European Union–NextGenerationEU. Award No.: Project code PE00000021, Concession Decree No. 1561 adopted on October 11, 2022 by the Italian Ministry of University and Research (MUR), CUP F53C22000770007, Project title "NEST - Network 4 Energy Sustainable Transition".

DATA AVAILABILITY

The data that support the findings of this article are not publicly available. The data are available from the authors upon reasonable request.

[1] A. Kane, V. Verma, and B. Singh, Renew. Sustain. Energy Rev. **75**, 1295 (2017).
[2] Z. Tong, Y. Zhang, T. Frauenheim, and T. Dumitrică, Nano Lett. **25**, 7283 (2025).
[3] G. A. Slack, in *CRC Handbook of Thermoelectrics*, edited by D. M. Rowe (CRC Press, Boca Raton, FL, 1995), pp. 407–440.
[4] A. F. Ioffe, *Semiconductor Thermoelements and Thermoelectric Cooling* (Infosearch, London, 1958).
[5] A. M. A. Leguy, A. R. Goñi, J. M. Frost, J. M. Skelton, F. Brivio, X. Rodríguez-Martínez, O. J. Weber, A. Pallipurath, M. I. Alonso, M. Campoy-Quiles *et al.*, Phys. Chem. Chem. Phys. **18**, 27051 (2016).
[6] M. Songvilay, N. Giles-Donovan, M. Bari, Z.-G. Ye, J. L. Minns, M. A. Green, G. Xu, P. M. Gehring, K. Schmalzl, W. D. Ratcliff, C. M. Brown, D. Chernyshov, W. van Beek, S. Cochran, and C. Stock, Phys. Rev. Mater. **3**, 093602 (2019).
[7] L. D. Whalley, J. M. Skelton, J. M. Frost, and A. Walsh, Phys. Rev. B **94**, 220301(R) (2016).
[8] C. Mao, X. He, H.-M. Lin, M. K. Gupta, P. Postec, T. Lanigan-Atkins, M. Krogstad, D. M. Pajerowski, T. Hong, T. J. Williams, J. R. Stewart, D. Y. Chung, M. G. Kanatzidis, S. Rosenkranz, R. Osborn, and O. Delaire, Phys. Rev. Mater. **9**, 065401 (2025).
[9] H. Xie, S. Hao, J. Bao, T. J. Slade, G. J. Snyder, C. Wolverton, and M. G. Kanatzidis, J. Am. Chem. Soc. **142**, 9553 (2020).
[10] L. A. Muscarella and E. M. Hutter, ACS Energy Lett. **7**, 2128 (2022).
[11] M. Sajjad, Q. Mahmood, N. Singh, and J. A. Larsson, ACS Appl. Energy Mater. **3**, 11293 (2020).
[12] A.H. Slavney, L. Leppert, A. Saldivar-Valdes, D. Bartesaghi, T. J. Savenije, J. B. Neaton, and H. I. Karunadasa, Angew. Chem. Int. Ed. **57**, 12765 (2018).
[13] G. J. Snyder and E. S. Toberer, Nat. Mater. **7**, 105 (2008).
[14] C. Fu, S. Bai, Y. Liu, X. Zhao, and T. Zhu, Nat. Commun. **6**, 8144 (2015).
[15] R. Chen, H. Kang, R. Min, Z. Chen, E. Guo, X. Yang, and T. Wang, Internat. Mater. Rev. **69**, 83 (2024).
[16] B. C. Sales, D. Mandrus, and R. K. Williams, Science **272**, 1325 (1996).
[17] G. S. Nolas, J. Sharp, and H. J. Goldsmid, *Thermoelectrics: Basic Principles and New Materials Developments* (Springer, New York, 2001).
[18] E. Di Lucente, M. Simoncelli, and N. Marzari, Phys. Rev. Res. **5**, 033125 (2023).
[19] M. Christensen, S. Johnsen, and B. B. Iversen, Dalton Trans. **39**, 978 (2010).
[20] M. Ohnishi, T. Yamamoto, K. Fujimura, H. Shimizu, K. Yamamoto, and J. Shiomi, Chem. Mater. **36**, 10595 (2024).
[21] M. H. R. Aslam, Chem. Inorg. Mater. **7**, 100118 (2025).
[22] M. González-Barrios, M. Tabuyo-Martínez, D. Ávila-Brande, and J. Prado-Gonjal, Small Structures **5**, 2400136 (2024).
[23] T. Takabatake, K. Suekuni, T. Nakayama, and E. Kaneshita, Rev. Mod. Phys. **86**, 669 (2014).

[24] Y. Lu, S. Chen, W. Wu, Z. Du, Y. Chao, and J. Cui, Sci. Rep. **7**, 40224 (2017).

[25] N. Cheng, R. Liu, S. Bai, X. Shi, and L. Chen, J. Appl. Phys. **115**, 163705 (2014).

[26] H. Ming, Z.-Z. Luo, Z. Zou, and M.G. Kanatzidis, Chem. Rev. **125**, 3932 (2025).

[27] H. Xie, X. Su, S. Hao, C. Zhang, Z. Zhang, W. Liu, Y. Yan, C. Wolverton, X. Tang, and M.G. Kanatzidis, J. Am. Chem. Soc. **141**, 18900 (2019).

[28] J. Zhang, R. Liu, N. Cheng, Y. Zhang, J. Yang, C. Uher, X. Shi, L. Chen, and W. Zhang, Adv. Mater. **26**, 3848 (2014).

[29] L. Huang, Y. Li, S. Sha, B. Ge, Y. Wu, J. Yan, Y. Kong, and J. Zhang, Small **19**, 2206865 (2023).

[30] H.-J. Wu and Z. Jin Dong, Acta Mater. **118**, 331 (2016).

[31] A. Cappai, C. Melis, D. Marongiu, F. Quochi, M. Saba, F. Congiu, Y. He, T. J. Slade, M.G. Kanatzidis, and L. Colombo, Adv. Sci. **11**, 2305861 (2024).

[32] A. Cappai, C. Melis, and L. Colombo, Phys. Rev. Mater. **9**, 054605 (2025).

[33] S. I. Tamura, Phys. Rev. B **27**, 858 (1983).

[34] R. Gurunathan, R. Hanus, M. Dylla, A. Katre, and G. J. Snyder, Phys. Rev. Appl. **13**, 034011 (2020).

[35] B. R. Nag, *Electron Transport in Compound Semiconductors* (Springer Science & Business Media, Berlin, Heidelberg, 2012), Vol. 11.

[36] J. M. Ziman, *Electrons and Phonons: The Theory of Transport Phenomena in Solids* (Oxford University Press, Oxford, 2001).

[37] H. Brooks, in *Advances in Electronics and Electron Physics* (Elsevier, Amsterdam, 1955), Vol. 7, pp. 85–182.

[38] J. Callaway, Phys. Rev. **113**, 1046 (1959).

[39] H. Kosina and G. Kaiblinger-Grujin, Solid-State Electron. **42**, 331 (1998).

[40] E. Conwell and V. F. Weisskopf, Phys. Rev. **77**, 388 (1950).

[41] J. Leveillee, X. Zhang, E. Kioupakis, and F. Giustino, Phys. Rev. B **107**, 125207 (2023).

[42] H. Lee, S. Poncé, K. Bushick, S. Hajinazar, J. Lafuente-Bartolome, J. Leveillee, C. Lian, J.-M. Lihm, F. Macheda, H. Mori *et al.*, npj Comput. Mater. **9**, 156 (2023).

[43] W. Kohn and J. M. Luttinger, Phys. Rev. **108**, 590 (1957).

[44] Y. Peter and M. Cardona, *Fundamentals of Semiconductors: Physics and Materials Properties* (Springer Science & Business Media, Berlin, Heidelberg, 2010).

[45] E. F. Schubert, MRS Proc. **340**, 273 (1994).

[46] M. D. McCluskey and E. E. Haller, *Dopants and Defects in Semiconductors* (CRC Press, Boca Raton, FL, 2018).

[47] L. M. C. Pereira, U. Wahl, S. Decoster, J. G. Correia, L. M. Amorim, M. R. da Silva, J. P. Araújo, and A. Vantomme, Phys. Rev. B **86**, 125206 (2012).

[48] X. Wang, M. Zhang, T. Hou, X. Sun, and X. Hao, Small **19**, 2303060 (2023).

[49] J. Cao, S. X. Tao, P. A. Bobbert, C.-P. Wong, and N. Zhao, Adv. Mater. **30**, 1707350 (2018).

[50] Y. Zhao, I. Yavuz, M. Wang, M. H. Weber, M. Xu, J.-H. Lee, S. Tan, T. Huang, D. Meng, R. Wang *et al.*, Nat. Mater. **21**, 1396 (2022).

[51] C. Wu, X.-L. Shi, L. Wang, W. Lyu, P. Yuan, L. Cheng, Z.-G. Chen, and X. Yao, ACS Nano **18**, 31660 (2024).

[52] H.-T. Xue, Z.-L. Hu, Y.-Q. Luo, J.-P. An, and F.-L. Tang, Mater. Res. Exp. **9**, 046304 (2022).

[53] N. Mingo, D. Hauser, N. P. Kobayashi, M. Plissonnier, and A. Shakouri, Nano Lett. **9**, 711 (2009).

[54] A. Seko, A. Takahashi, and I. Tanaka, Phys. Rev. B **90**, 024101 (2014).

[55] P. G. Klemens, Proc. Phys. Soc. A **68**, 1113 (1955).

[56] P. G. Klemens, Phys. Rev. **119**, 507 (1960).

[57] C. Ratsifaritana and P. Klemens, Int. J. Thermophys. **8**, 737 (1987).

[58] N. Mingo and D. A. Broido, Nano Lett. **5**, 1221 (2005).

[59] P. Giannozzi, Jr., O. Andreussi, T. Brumme, O. Bunau, M. B. Nardelli, M. Calandra, R. Car, C. Cavazzoni, D. Ceresoli, M. Cococcioni *et al.*, J. Phys.: Condens. Matter **29**, 465901 (2017).

[60] P. Giannozzi, S. Baroni, N. Bonini, M. Calandra, R. Car, C. Cavazzoni, D. Ceresoli, G. L. Chiarotti, M. Cococcioni, I. Dabo *et al.*, J. Phys.: Condens. Matter **21**, 395502 (2009).

[61] S. Poncé, E. Margine, C. Verdi, and F. Giustino, Comput. Phys. Commun. **209**, 116 (2016).

[62] T. Tadano and S. Tsuneyuki, Phys. Rev. B **92**, 054301 (2015).

[63] T. Tadano, Y. Gohda, and S. Tsuneyuki, J. Phys.: Condens. Matter **26**, 225402 (2014).

[64] G. K. Madsen, J. Carrete, and M. J. Verstraete, Comput. Phys. Commun. **231**, 140 (2018).

[65] M. Lundstrom, *Fundamentals of Carrier Transport*, 2nd ed. (Cambridge University Press, Cambridge, 2000).

[66] R. Dettori, A. Cappai, C. Melis, and L. Colombo, Nano Express **6**, 045004 (2025).

[67] X. Chen, Y. Pan, Y. Ding, H. Lian, J. Lin, and L. Li, Inorg. Chem. **63**, 3525 (2024).

[68] L. Lindsay, D. A. Broido, and T. L. Reinecke, Phys. Rev. B **87**, 165201 (2013).

[69] Z. Yang, A. Rajagopal, C. -C. Chueh, and A. K. -Y. Jen, Adv. Mater. **30**, 1803230 (2018).

[70] B. Saparov and D. B. Mitzi, Chem. Rev. **116**, 4558 (2016).

[71] T. Pandey, M. -H. Du, D. S. Parker, and L. Lindsay, Mater. Today Phys. **28**, 100881 (2022).

[72] A. Pisoni, J. Jacimovic, O. S. Barišić, M. Spina, R. Gaál, L. Forró, and M. Horvatić, J. Phys. Chem. Lett. **7**, 2486 (2016).

[73] X. Yan, W. Liu, S. Chen, H. Wang, L. Chen, and G. J. Snyder, Nature (London) **489**, 414 (2012).

[74] S. Chen and Z. Ren, Mater. Today **16**, 387 (2013).

[75] M. A. Haque, S. Kee, D. R. Villalva, W.-L. Ong, and D. Baran, Adv. Sci. **7**, 1903389 (2020).

[76] T. Liu, X. Zhao, J. Li, Z. Liu, F. Liscio, S. Milita, B. C. Schroeder, and O. Fenwick, Nat. Commun. **10**, 5750 (2019).

[77] S. Saini, A. K. Baranwal, T. Yabuki, S. Hayase, and K. Miyazaki, MRS Advances **4**, 1719 (2019).

[78] W. Lee, H. Li, A. B. Wong, D. Zhang, M. Lai, Y. Yu, Q. Kong, E. Lin, J. J. Urban, J. C. Grossman *et al.*, Proc. Natl. Acad. Sci. USA **114**, 8693 (2017).

[79] P. Bhumla, M. Jain, S. Sheoran, and S. Bhattacharya, J. Phys. Chem. Lett. **13**, 11655 (2022).

[80] H. U. Rehman, M. Jamil, N. Wang, G. Murtaza, M. Shafiq, M. Usman, Z. Usman, M. Zulfiqar, and M. A. Khan, Mater. Today Commun. **40**, 109806 (2024).